AGU PUBLICATIONS

Journal of Advances in Modeling Earth Systems

RESEARCH ARTICLE

10.1002/2015MS000568

The role of precipitation and spatial organization in the response of trade-wind clouds to warming

Raphaela Vogel[1], Louise Nuijens[1,2], and Bjorn Stevens[1]

[1]Max Planck Institute for Meteorology, Hamburg, Germany, [2]Department of Earth, Atmospheric and Planetary Sciences, Massachusetts Institute of Technology, Cambridge, Massachusetts, USA

Key Points:
- Cloud cover and albedo reduce only slightly with warming, demonstrating the robustness of shallow cumuli
- Precipitation prevents warmer cloud layer from deepening and relative drying
- Strong sensitivity of trade-wind boundary layer to presence of deeper convection

Correspondence to:
R. Vogel,
raphaela.vogel@mpimet.mpg.de

Citation:
Vogel, R., L. Nuijens, and B. Stevens (2016), The role of precipitation and spatial organization in the response of trade-wind clouds to warming, *J. Adv. Model. Earth Syst.*, *8*, doi:10.1002/2015MS000568.

Received 19 OCT 2015
Accepted 3 MAY 2016
Accepted article online 6 MAY 2016

Abstract Using highly resolved large-eddy simulations on two different domain sizes, we investigate the influence of precipitation and spatial organization on the thermodynamic structure of the trade-wind layer, under a uniform 4 K warming at constant relative humidity. In nonprecipitating simulations, the increased surface latent heat flux in the warmer climate produces a deeper and drier cloud layer with reduced cloud fractions between 1.5 and 4 km. Precipitation prevents the deepening and drying of the cloud layer in response to warming. Cloud fractions still decrease in the upper cloud layer, because stratiform outflow layers near cloud tops are less pronounced and because the larger liquid water contents are confined to narrower updrafts. Simulations on a 16-fold larger domain lead to the spatial organization of clouds into larger and deeper cloud clusters. The presence of deeper clouds results in a shallower, warmer, and drier trade-wind layer, with strongly reduced cloud cover. The warming response in the precipitating large-domain simulation nevertheless remains similar to the small-domain precipitating simulation. On the large domain, deeper clouds can also develop without precipitation, because moisture-convection feedbacks strengthen in the absence of cold-pool dynamics. Overall, total cloud cover and albedo decrease only slightly with warming in all cases. This demonstrates the robustness of shallow cumuli—in particular of cloud fraction near the lifting condensation level—to changes in the large-scale environment.

1. Introduction

Shallow trade-wind cumuli in regimes with moderately subsiding large-scale vertical motion have been recognized as a critical source of uncertainty in projections of future climate [e.g., *Bony and Dufresne*, 2005; *Vial et al.*, 2013]. Covering a large fraction of the world's oceans, these marine boundary layer clouds are decisive for climate change not only through their impact on the shortwave radiation budget, but also for their role in driving atmospheric circulations, both by modulating surface evaporation [e.g., *Tiedtke*, 1989; *Stevens*, 2007] and by influencing the distribution of longwave cooling within the atmosphere [*Muller and Held*, 2012; *Emanuel et al.*, 2014; *Fermepin and Bony*, 2014]. Most comprehensive climate models indicate a reduction of cloud cover in response to warming and thus a positive low cloud feedback; because of insufficient physical understanding, however, confidence in these results remains low [*Boucher et al.*, 2013].

Because of uncertainties in the parameterization of boundary layer clouds in climate models, other tools are required to advance understanding of how low clouds change in response to climate perturbations. High-resolution models like LES promote process-level understanding, because they explicitly resolve motions on the scale of the larger boundary layer eddies. Using LES, *Rieck et al.* [2012] introduced the idea that due to increasing surface latent heat fluxes, the cloud layer deepens and, by enhanced entrainment of dry free tropospheric air, becomes relatively drier. This drying reduces the cloud cover which, all else being equal, would constitute a positive cloud feedback in the shallow cumulus regime. The simple study design, using a uniform temperature increase at constant relative humidity, revealed a new mechanism influencing cloud feedbacks. But this approach also had limitations, most significantly perhaps its neglect of precipitation.

Observations show that trade-wind cumuli precipitate frequently [e.g., *Short and Nakamura*, 2000; *Nuijens et al.*, 2009; *Burdanowitz et al.*, 2015]. Precipitation changes the microphysical structure of the shallow clouds and influences the energetics of the trade-wind boundary layer, including the heating and moistening tendencies and the growth rate of the boundary layer (here including both the subcloud and the trade-wind cloud layer). Because precipitation removes liquid water available for evaporation at cloud top, it limits

cloud layer deepening [*Albrecht*, 1993; *Stevens and Seifert*, 2008; *VanZanten et al*., 2011; *Bretherton et al*., 2013]—an important mechanism in the response of shallow cumulus to idealized climate perturbations [*Blossey et al*., 2013; *Bretherton et al*., 2013]. Precipitation also affects cloud amount and cloud organization, through the emergence of cold pools [e.g., *Zuidema et al*., 2012; *Seifert and Heus*, 2013]. Here we ask if the response of cloudiness to warming differs as a result of allowing shallow convection to precipitate, a question motivated by the effect of precipitation on both the spatial structure of convection and the rate of convective deepening.

To investigate the response of clouds to warming in the presence of precipitation, we perform simulations on relatively large domains, because this has been shown to influence the degree to which convection organizes [e.g., *Muller and Held*, 2012; *Seifert and Heus*, 2013]. Much deeper convection emerges in simulations supporting convective organization, which provides an opportunity to study the response of clouds to warming in a more convective regime. By contrasting the warming response of clouds in the large domain, in which deeper convection arises, with that in a smaller domain, it is also possible to ask to what extent the depth of convective mixing influences the cloud response to warming, as has been hypothesized in some recent studies [*Sherwood et al*., 2014; *Zhao*, 2014].

We study the effect of an idealized climate change on precipitating shallow convection by applying a uniform warming to the initial temperature profile in a constant relative humidity framework, similar to *Rieck et al*. [2012]. An idealized approach helps clarify the physical effects at play in the simplest possible setting. This has advantages and disadvantages. For instance, the idealizations may distort the response of clouds to climate change by leaving out important cloud-controlling factors such as wind shear, increases in free-tropospheric stability, changes in the CO_2 concentration, in longwave cooling, subsidence strength, or inversion stability [e.g., *Bretherton et al*., 2013]. Thus, our results should not be considered as a quantification of cloud feedbacks, but rather as an attempt to understand a particular problem that is relevant for climate change.

The structure of the paper is as follows. The LES code, the model setup, and the experiment design are discussed in section 2. Section 3 investigates the impact of precipitation on the trade-wind boundary layer. How precipitation modulates the warming response is discussed in section 4. In section 5, we use large domain simulations to study the impact of deeper (and arguably more aggregated) convection on both the thermodynamic structure of the trade-wind layer and its response to warming. Concluding remarks are presented in section 6.

2. Large-Eddy Simulation

We perform LES with the University of California Los Angeles (UCLA) LES code [*Stevens et al*., 2005] in a setup representative of the conditions in the broader trades. In contrast to *Rieck et al*. [2012] who used the RICO case study described by *VanZanten et al*. [2011], we adopt the framework of *Bellon and Stevens* [2012]. The framework has been used to study nonprecipitating stratocumulus and shallow cumulus convection in contrasting large-scale environments [*Bellon and Stevens*, 2012; *Nuijens and Stevens*, 2012; *Bellon and Geoffroy*, 2016]. Our motivation for this change is twofold: (a) it allows us to test the generality of the *Rieck et al*. [2012] results, and (b) brings the simulation closer to equilibrium as the free-tropospheric tendencies are strictly balanced. Achieving an equilibrium is particularly important with precipitation whose intermittent nature necessitates long averaging times (and/or very large domains).

2.1. LES Code

The UCLA LES solves the Ogura-Phillips anelastic equations with prognostic equations for the three wind components and two thermodynamic variables, the liquid water potential temperature (θ_l), and the total water mixing ratio (q_t), which includes vapor and cloud water. A third-order Runge-Kutta time integration is used with variable time step (1 s or less to satisfy the Courant-Friedrichs-Lewy criterion). Momentum advection is based on fourth-order centered differences, while a higher-order upwind method with monotone centered slope limiters is applied to advect the scalars. The subgrid scale fluxes are modeled with the Smagorinsky-Lilly model.

Liquid water content is diagnosed according to a saturation adjustment scheme. Precipitating simulations are performed with the two-moment warm rain scheme of *Seifert and Beheng* [2001], assuming a constant

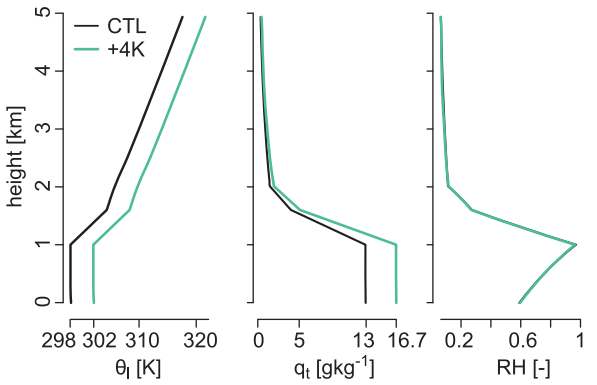

Figure 1. Initial profiles of the liquid water potential temperature θ_l, total humidity q_t, and relative humidity *RH*, for the CTL and +4K climate states.

cloud droplet number concentration $N_c = 50$ cm^{-3} (representing clean maritime conditions at the lower end of observations [*Siebert et al.*, 2013]) and solving two additional prognostic equations for rain mass and number concentration. A more detailed description of the cloud microphysical model is provided by *Savic-Jovcic and Stevens* [2008].

2.2. Model Setup and Experiment Design

The framework we use prescribes large-scale forcings and initial profiles characteristic for the broader trades. Wind shear, which may be important for regulating mixing and projected cloud cover, is not prescribed in this study. Some shear develops in the lowest 1.5 km (see Figure 4), but we do not attempt to address here how shear, or changes in shear, might modify the response of clouds to warming. The setup uses a Eulerian reference frame with homogeneous large-scale forcings (fixed sea surface temperature (SST) and subsidence). The forcings are prescribed as follows:

1. Subsidence: exponential profile with maximum value of $w_0 = 7.5 \times 10^{-3}$ m s^{-1}
2. Radiative cooling: uniform cooling of $Q_R = -2.5$ K d^{-1}
3. Wind speed: a barotropic geostrophic wind of 10 m s^{-1} aligned with the *x*-coordinate of the domain

Both the subsidence rate and the radiative cooling are relatively large compared to other case setups, but help compensate for the lack of additional drying and cooling from horizontal advection.

The initial temperature and humidity profiles (Figure 1) have a well-mixed subcloud layer, topped by an inversion layer. The free-tropospheric temperature lapse rate is chosen such that subsidence warming balances radiative cooling. Bulk aerodynamic formulas parameterize the surface thermodynamic and momentum fluxes, with constant SST and a slip/no-penetration condition. Integrations are performed with a horizontal grid spacing of 50 m and a vertical grid spacing uniformly stretched by a factor of 1.02 from 10 m at the surface to about 200 m at the domain top at 10 km.

Table 1 provides an overview of the experiments performed (the focus lies on the upper seven simulations; the additional sensitivity experiments will be referred to in section 5 and Appendix A). We distinguish the control (CTL) and the warmed (+4K) climate state, the nonprecipitating and precipitating cases on the small

Table 1. Specifications Used for the Different Perturbation Experiments

Case Name	SST (K)	θ_l Profile	q_t Profile	Precipitation	Domain (km^3)	radiation
noP-CTL	300	CTL	CTL	Off	12.8 × 12.8 × 10	Uniform
noPlarge-CTL	300	CTL	CTL	Off	51.2 × 51.2 × 10	Uniform
P-CTL	300	CTL	CTL	On	12.8 × 12.8 × 10	Uniform
Plarge-CTL	300	CTL	CTL	On	51.2 × 51.2 × 10	Uniform
noP+4K	304	+4 K	Adjusted	Off	12.8 × 12.8 × 10	Uniform
P+4K	304	+4 K	Adjusted	On	12.8 × 12.8 × 10	Uniform
Plarge+4K	304	+4 K	Adjusted	On	51.2 × 51.2 × 10	Uniform
Additional sensitivity experiments:						
P-4K	296	−4 K	Adjusted	On	12.8 × 12.8 × 10	Uniform
Plarge-4K	296	−4 K	Adjusted	On	51.2 × 51.2 × 10	Uniform
Δ seeds [3×]	300	CTL	CTL	On	12.8 × 12.8 × 10	Uniform
(102.4km)^2	300	CTL	CTL	On	102.4 × 102.4 × 10	Uniform
IRAD Plarge	300	CTL	CTL	On	51.2 × 51.2 × 10	Interactive[a]

[a]A similar implementation as in *Seifert et al.* [2015] is used for interactive radiation, which is based on the broadband radiation code of *Fu and Liou* [1992] and uses Monte Carlo spectral Integration [*Pincus and Stevens*, 2009].

12.8 × 12.8 km^2 domain (noP and P) and on the 16-fold larger 51.2 × 51.2 km^2 domain (Plarge and noPlarge). The difference between the two climate states is a uniform 4 K shift of the temperature profile in the +4K case compared to the CTL, along with an equivalent SST increase. The +4K humidity profile is adjusted such that the initial profile of the relative humidity is not changed. For both climate states, a precipitating and a nonprecipitating simulation is performed on the small domain.

To allow deeper clouds to form, we perform additional precipitating simulations of both the CTL and +4K climate state on the larger domain which allows for shallow convective organization. To test whether convection organizes in the absence of cold pools, the nonprecipitating CTL simulation is also performed on the large domain. As indicated in the introduction, some of the large-domain simulations produce relatively deep clouds reaching beyond the freezing level and up to the domain top. To prevent these simulations from accumulating liquid at the top, a nudging toward the initial q_t-profiles is applied in the six highest model levels, beginning at 8.8 km. Ice processes, which become increasingly relevant for clouds above 8 km in the tropics, are not considered. Because our focus is on shallow convection, and we merely use the simulations that develop deeper convection to explore its effect on the structure of the shallower clouds, we do not believe that this admittedly artificial treatment unduly influences the interpretations we draw from the simulations.

Because precipitation and domain size strongly determine the time to reach quasi-stationarity, if reached at all, different averaging periods are used to present the statistics, namely day 7–10 for P-CTL and P+4K, day 2.5–4 for Plarge-CTL and Plarge+4K, and day 7 and 8 (in section 3) or day 7 only (section 4) for noP-CTL and noP+4K.

3. The Importance of Precipitation for Attaining an Equilibrium

In this section, we document the influence of precipitation on the thermodynamic structure of the simulated trade-wind boundary layer and present a comparison of the baseline behavior of the precipitating and nonprecipitating control simulations on the small domain. In terms of the general evolution of the flow, a shallow layer of cumulus develops after a few hours of simulation time (Figure 2). This layer progressively deepens, reaching a depth of about 2250 m after two simulation days with a total cloud cover of 12.5% and mean cloud base near 600 m. The surface fluxes evolve more slowly, with surface sensible and latent heat fluxes of, respectively, −1.8 and 300 W m^{-2} after 2 days, while the latter decreases to a value around 250 W m^{-2} after 8 days. The negative value of the sensible heat flux is caused by entraining warmer cloud layer air into the well-mixed subcloud layer in the absence of sufficient radiative or horizontal-advective cooling, which reduces the temperature gradient with respect to the underlying SST. Relatively deep cloud layers develop in our simulations with surface latent heat fluxes that are larger than measured during the BOMEX campaign [see e.g., *Holland and Rasmusson*, 1973], but not far from RICO observations when latent heat fluxes as strong as 250 W m^{-2} were measured [*Zuidema et al*., 2012; *Nuijens et al*., 2009]. One reason for the large latent heat fluxes of both the P-CTL and noP-CTL simulations is the on average 1–2 g kg^{-1} drier initial humidity profile in the lower free troposphere compared to other trade-wind cumulus cases [*VanZanten et al*., 2011; *Bellon and Stevens*, 2012]. The reduced free-tropospheric humidity enhances the drying of the boundary layer through cloud-top entrainment and—rather than suppressing convection as one may expect—increases the vigor of convection through a larger surface buoyancy flux.

The time series (Figure 2) show that the P-CTL and noP-CTL simulations have a similar boundary layer depth, surface fluxes, and cloud properties until the cloud layer is deep enough for the shallow clouds to produce substantial precipitation on the order of 0.5 mm d^{-1} (∼15 W m^{-2}) after 4 days. As soon as substantial precipitation sets in, the cloud layer ceases to deepen further. The noP-CTL simulation does not reach stationarity and cloud cover continues to increase with time, especially toward the end of the simulation when pronounced stratiform outflows are formed. In P-CTL, however, the onset of precipitation stops the steady increase of cloud cover, which reaches a value of 13.5% in equilibrium. The P-CTL time series show marked oscillations: the domain size of 12.8 × 12.8 km^2 only supports one or two larger precipitating clouds which leave an imprint on the time series (such variations are much less pronounced on the larger domain).

Precipitation removes liquid that would otherwise evaporate and deepen the cloud layer—a mechanism that is both understood theoretically [*Stevens*, 2007] and evident in models with different degrees of complexity [*Albrecht*, 1993; *Stevens and Seifert*, 2008; *VanZanten et al*., 2011; *Bretherton et al*., 2013]. Reaching an

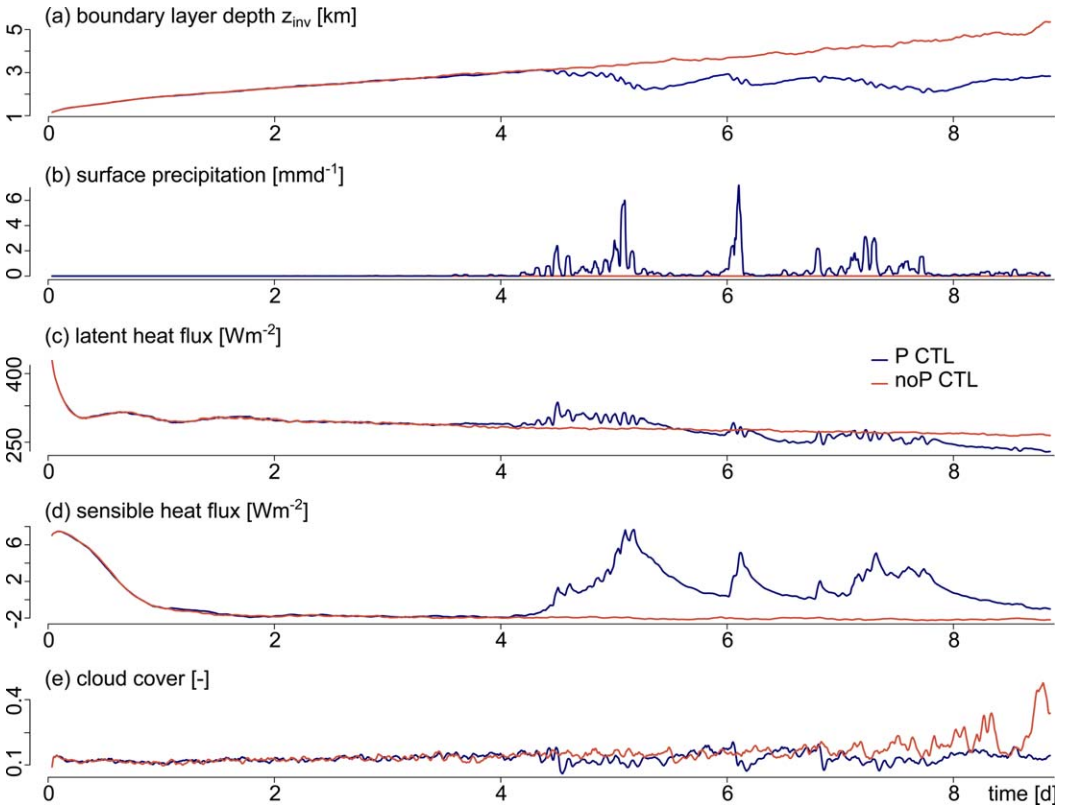

Figure 2. Domain-averaged time series for P-CTL (dark blue) and noP-CTL (red).

equilibrium state, including a halt of boundary layer growth, requires that the heating and moistening tendencies are in balance throughout the layer. The following terms appear in the tendency equations, written in terms of the apparent heat sink Q_1 and moisture source Q_2 (following *Yanai et al*. [1973]):

$$Q_1 := -\left[\frac{\partial\overline{\theta_l}}{\partial t}\Big|_{tot} + \omega\frac{\partial\overline{\theta_l}}{\partial z}\Big|_{sub}\right] = -\frac{\partial\overline{\theta_l}}{\partial t}\Big|_{cnv} - \frac{\partial\overline{\theta_l}}{\partial t}\Big|_{prc} - Q_R \tag{1}$$

$$Q_2 := \frac{L}{c_p}\left[\frac{\partial\overline{q_t}}{\partial t}\Big|_{tot} + \omega\frac{\partial\overline{q_t}}{\partial z}\Big|_{sub}\right] = \frac{L}{c_p}\left[\frac{\partial\overline{q_t}}{\partial t}\Big|_{cnv} + \frac{\partial\overline{q_t}}{\partial t}\Big|_{prc}\right] \tag{2}$$

where the terms on the left-hand side are the storage term or total tendency and large-scale subsidence. The terms on the right-hand side represent the contributions from convection (which is the turbulent flux divergence that represents the resolved and subgrid-scale components of the simulated flow), precipitation and, in case of θ_l, the prescribed radiative cooling Q_R. Overbars stand for horizontal (slab) averages. To convert g kg^{-1} to K d^{-1}, the moistening tendencies are multiplied by the enthalpy of vaporization L and divided by the isobaric-specific heat capacity of dry air c_p. Given the choice of the thermodynamic variables as θ_l and q_t, the condensation and evaporation of cloud droplets do not affect the heat and moisture budget. For precipitation processes, however, θ_l (following its formulation in the LES) and q_t are not conserved and the formation and evaporation of precipitation represent a heating/drying and a cooling/moistening, respectively. Note that we inverted the signs of Q_1 and Q_2 compared to *Yanai et al*. [1973], as shallow convection mainly acts as a source of moisture rather than a sink. Because Q_R is constant, Q_1 is shown without the radiative contribution (that is, $Q_1 + Q_R$).

Figure 3 illustrates how the boundary layer state is maintained by the different processes. In noP-CTL, the balance in the inversion layer, located here around 4.2 km, is given by the uniform radiative cooling, large-scale subsidence and convection. At the inversion, the warm and dry subsiding air meets with the moist and cold air lofted by convection. This leads to a maximum of both subsidence warming and drying, and convective cooling and moistening. In the specified large-scale environment, subsidence is not strong enough to counteract the convective tendencies, and a strong residual tendency remains that cools and

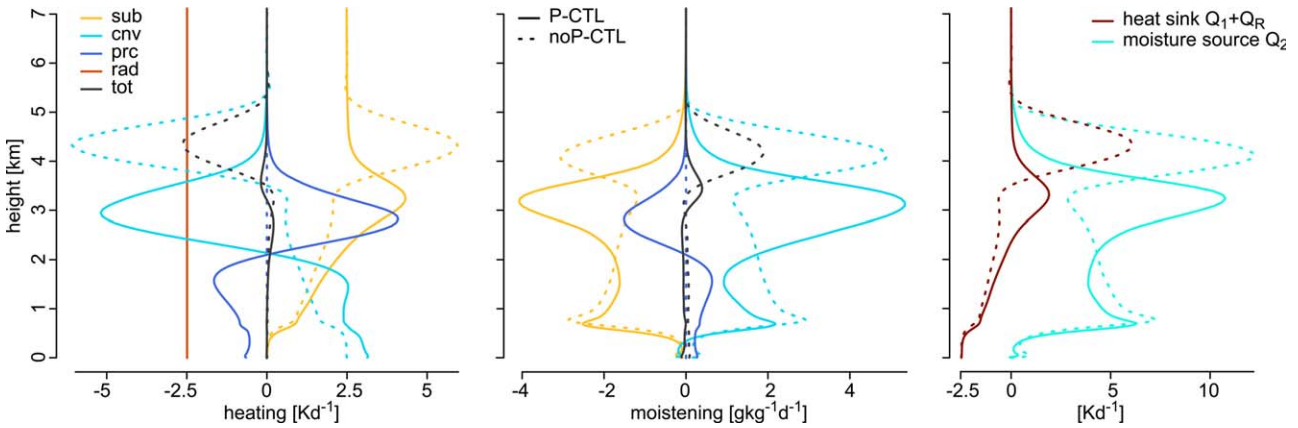

Figure 3. (left and middle) Vertical profiles of domain-averaged contributions of the tendency equation terms for θ_l (heating) and q_t (moistening), and (right) the profiles of the heat sink (Q_1+Q_R) and moisture source (Q_2). Shown are P-CTL (solid) and noP-CTL (dashed, averaged over day 7 and 8).

moistens the inversion layer (the residual moistening tendency integrated over the whole boundary layer amounts to 47 Wm^{-2}, see Table 2). As convection keeps destabilizing the inversion layer and increasing the depth of the cloud layer, the boundary layer deepens [*Betts*, 1973; *Stevens*, 2007].

Precipitation has an opposing tendency to convection in the inversion layer. The heating and drying induced by precipitation formation limits boundary layer deepening and leads to a negligible residual integrated moistening tendency of 1 Wm^{-2} (Table 2). The right plot of Figure 3 shows the apparent heat sink (Q_1+Q_R) and moisture source (Q_2). The heat sink in the inversion layer is strongly reduced due to the heating tendency of precipitation. Also the Q_2 maxima in the inversion layer and near the cumulus bases around 700 m are somewhat smaller in P-CTL. The evaporation of precipitation provides a cooling and moistening over much of the cloud layer, which goes along with reduced convective moistening in the lower cloud layer compared to noP-CTL. The resulting temperature and humidity profiles (Figure 4) show that the lapse rates change in the shallower precipitating cloud layer, with stronger temperature and weaker humidity lapse rates. As such, subsidence warming increases and subsidence drying decreases below about 2.5 km (see Figure 3).

VanZanten et al. [2011] noted the same behavior of the temperature and humidity profiles in precipitating LES of the RICO case, and also found that much of the evaporation of precipitation is concentrated in the cloud layer and not merely confined to the subcloud layer. *Albrecht* [1993] reported a similar effect of precipitation on the temperature stratification of the cloud layer. The cloud layer in his model, however, became drier, likely because the evaporation of precipitation was confined to the subcloud layer. Different microphysics schemes of different LES codes tend to produce very different precipitation flux (and cloud fraction) profiles, particularly if averaged over a few hours only [*VanZanten et al*., 2011; *Li et al*., 2015]. Investigating the influence of cloud droplet number concentration N_c on precipitating shallow convection, *Seifert et al*. [2015] find that all simulations reach a similar near-equilibrium rain rate. The main response to larger N_c is a delayed onset of rain, along with a slight deepening and drying of the cloud layer. So even if the

Table 2. Averages of Surface Latent Heat Flux (LHF), Changes in LHF With Warming (ΔLHF), the Surface Precipitation Rate (P_{surf}), Integrated Subsidence Drying (D), Integrated Residual Moistening Tendency (DT), Surface Sensible Heat Flux (SHF), Boundary Layer Depth (z_{inv}, Representing the Location of Maximum θ_l-Gradients), Cloud Cover (CC), Liquid Water Path (LWP), Albedo (α), Cloud Base Height (c_b), and Maximum Cloud Fraction ($cfrac_{max}$, Corresponding to the Maximum at Cloud Base); for the noP and P Simulations of Both the CTL and +4K Climate States[a]

Case	LHF ($W m^{-2}$)	ΔLHF (% K^{-1})	P_{surf}[b] ($W m^{-2}$)	D ($W m^{-2}$)	DT ($W m^{-2}$)	SHF ($W m^{-2}$)	z_{inv} (m)	CC (%)	LWP ($g m^{-2}$)	α (%)	c_b (m)	$cfrac_{max}$ (%)
noP-CTL	273	6.9	-	−226	47	−2.1	4116	16.2*	27.5*	10.7*	617	4.3
noP+4K	347	6.9	-	−282	64	−6.5	4940	15.3*	33.2*	10.5*	675	4.2
P-CTL	251	5.8	15	−236	1	0.7	2633	13.5	36.4	8.0	516	3.9
P+4K	310	5.8	16	−302	−8	−2.3	2056	11.9	40.6	7.1	528	3.7

[a]Values labeled with * denote averages taken over day 7 only, instead of day 7 and 8, to exclude biases introduced by the very deep cloud layer of the noP+4K simulation.
[b]Note that P_{surf} constitutes a negative contribution to the integrated moisture budget.

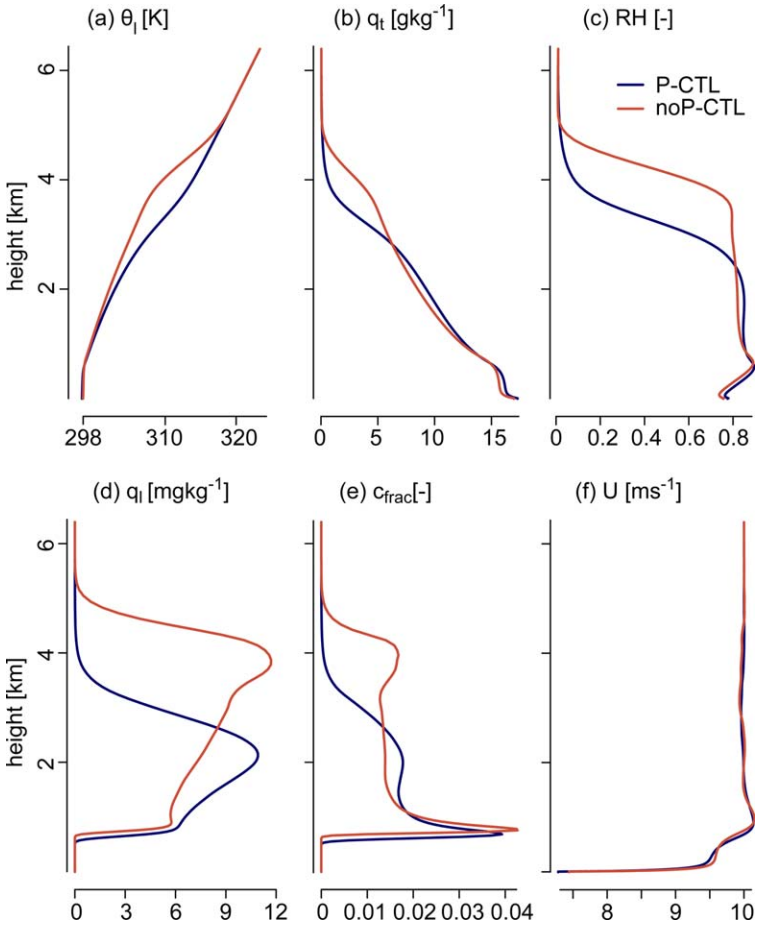

Figure 4. Domain-averaged vertical profiles of (a) the liquid water potential temperature θ_l, (b) total humidity q_t, (c) relative humidity *RH*, (d) domain-mean liquid water q_l, (e) cloud fraction c_{frac}, and (f) zonal wind speed *U*. Shown are P-CTL (dark blue) and noP-CTL (red, averaged over day 7 and 8).

cloud layer depth and the relative contribution of the different processes in the budgets depend slightly on N_c, the existing evidence suggests that N_c has little influence on the equilibrium response.

How do the changes of the thermodynamic structure in the presence of precipitation influence the clouds? The profiles of liquid water (Figure 4) show that the larger relative humidity in the cloud and subcloud layer results in more condensate-laden clouds with lower cloud bases. Although the precipitating cloud layer is shallower and liquid water is removed by precipitation, the liquid water path corresponding to the profiles displayed is 36.4 g m^{-2} in the P-CTL compared to 30.1 g m^{-2} in noP-CTL. In both cases, cloud fraction maximizes at cloud base and decreases with height through the cloud layer until the base of the inversion layer, where it increases slightly (depending on the case). Compared to noP-CTL, P-CTL has larger cloud fractions above cloud base, but total cloud cover, as defined by the number of cloudy columns, reduces to 13.5% compared to 17%, due to the clouds being shallower. Stronger wind shear would probably enhance the differences between the simulations, because the contribution of the deeper clouds (in noP-CTL) to projected cloud cover may increase in the presence of shear.

4. How Precipitation Modulates the Warming Response

What do the results of the previous section imply for the response of the precipitating simulation to warming? Here we use the simulations to address the hypothesis that if precipitation controls the depth of the boundary layer, the deepening and drying response to warming found in the nonprecipitating simulations of *Rieck et al.* [2012] is muted. To do so, we first consider the warming response in our nonprecipitating simulations.

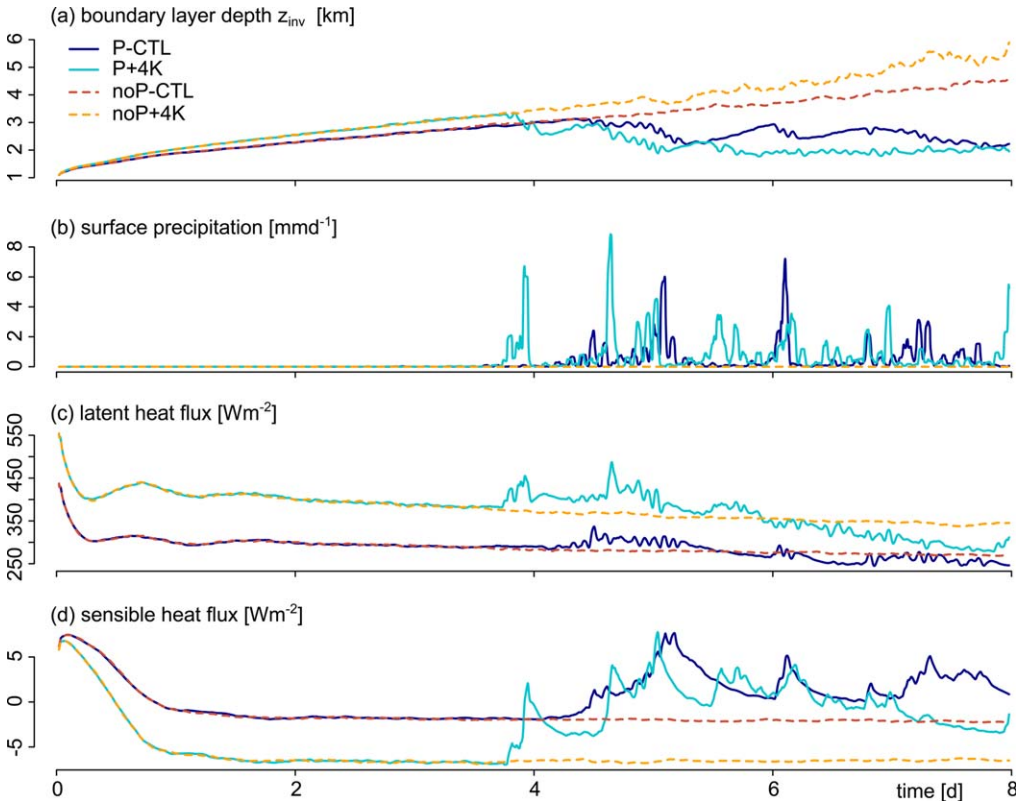

Figure 5. Domain-averaged time series of P (solid) and noP (dashed) for both the CTL and +4K climate states.

4.1. Nonprecipitating Warming Response

We find a similar response as *Rieck et al*. [2012] in the nonprecipitating simulations, namely an increase in surface latent heat flux, a decrease in sensible heat flux, a deepening of the cloud layer and reductions in cloud cover (Table 2 and Figure 5). The vertical profiles (Figure 6) indicate a slight relative drying associated with the deeper cloud layer of the noP+4K case: the relative humidity in the cloud layer between 1.5 and 4 km is slightly reduced, leading to reduced cloud fraction and liquid water at those heights. Because the relative humidity also reduces in the subcloud layer, cloud base rises by about 10%. How much a reduced cloud fraction between 1.5 and 4 km contributes to a reduction in total cloud cover may depend on how strongly clouds are sheared with height. Unlike in the RICO setup used by *Rieck et al*. [2012], the uniform wind in the present framework is associated with less shear (Figure 4f), but an unambiguous response to shear is not obvious. Rather than enhancing projected cloud cover, shear may also limit the lifetime of convective elements and reduce cloud cover. Despite clouds in the noP+4K case being deeper, the reduced cloud fraction between 1.5 and 4 km and less of a stratiform cloud component at cloud top lead to a ∼1% overall reduction of cloud cover (see Table 2). Because comparable reductions in cloud cover with warming occur in *Rieck et al*. [2012], it suggests that wind shear does not play a first-order role in the response of the simulations to warming. As the liquid water path is larger in noP+4K, the estimated albedo reduces only slightly, from 0.107 to 0.105. Here, the relation from *Zhang et al*. [2005] is used to approximate the albedo at a grid point by $\alpha=\tau/(6.8+\tau)$, with an optical depth estimate of $\tau=0.19\ \mathrm{LWP}^{5/6}\ \mathrm{N_c}^{1/3}$. Overall, it is worth bearing in mind how small the changes are.

Along with the small changes in cloudiness, the differences in the apparent heat sink (Q_1+Q_R) between the noP-CTL and noP+4K case are, except for the upward shift of the maximum, very small (Figure 7). This is because the initial temperature profile of the +4K case is shifted uniformly by 4 K and the lapse rate and thus subsidence warming are largely unaffected. Differences in the moisture source Q_2 are more pronounced throughout the cloud layer, because the initial absolute humidity profile of the +4K case is not uniformly shifted, but adjusted by the amount necessary to keep relative humidity constant. The differences

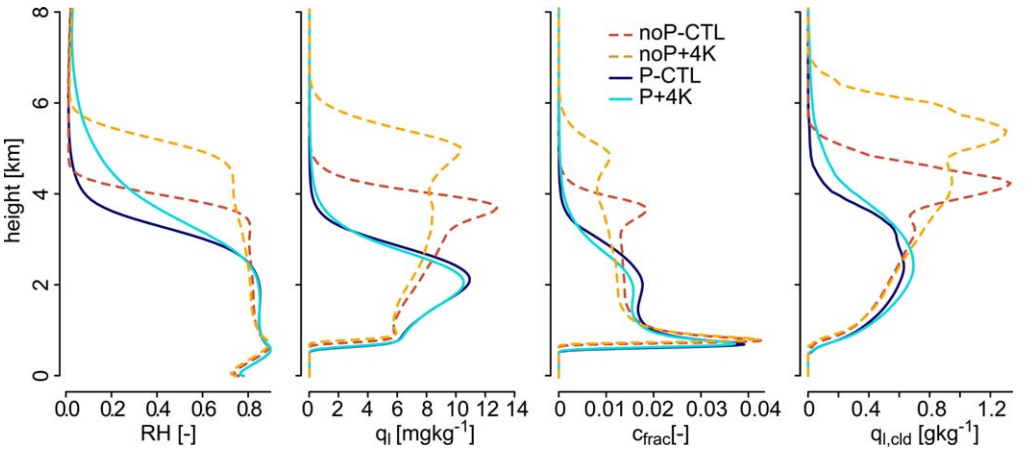

Figure 6. Domain-averaged profiles of relative humidity *RH*, domain-mean liquid water q_l, cloud fraction c_{frac}, and conditionally averaged cloud water $q_{l,cld}$. Shown are P (solid) and noP (dashed) for both the CTL and +4K climate states. The profiles for the P simulations are averages over day 7–10, the noP profiles are averages over day 7.

in humidity therefore vary from $\Delta q_t = 3.7$ g kg^{-1} at the surface to $\Delta q_t \approx 0$ g kg^{-1} at domain top. The vertical humidity gradient is thus enhanced and subsidence drying increases, which is balanced by more convective moistening (see also the integrated tendencies in Table 2). However, the additional moistening is only enough to compensate the enhanced subsidence drying in the cloud layer, and not the additional drying related to the redistribution of moisture across a deeper layer. Consequently, relative humidity decreases in the cloud layer in the +4K case.

4.2. Precipitating Warming Response

What about the warming response in the precipitating case? During the first 3.5 days before noticeable precipitation is found at the surface, the P+4K surface fluxes show the same behavior as in the noP+4K case and enhance boundary layer deepening compared to P-CTL (Figure 5). Because the clouds deepen more readily in P+4K, they precipitate sooner. In equilibrium, the P+4K boundary layer is shallower than P-CTL, and the differences in boundary layer depths is reduced compared to the noP cases (see Table 2). Also the differences in the surface fluxes between the two climate states are smaller than in the noP cases.

Although the mean cloud layer becomes even shallower in P+4K, the relative humidity in the cloud layer is very similar between P-CTL and P+4K (Figure 6). Also the subcloud layer relative humidity and the average

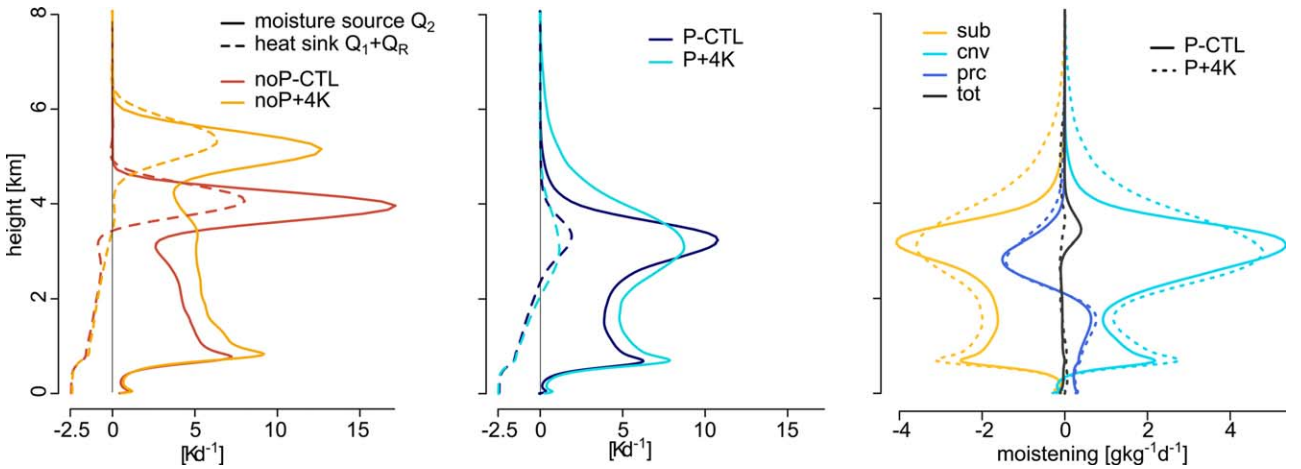

Figure 7. Profiles of the heat sink ($Q_1 + Q_R$, dashed) and moisture source (Q_2) for the CTL and +4K climate states of the noP cases (left, averages of day 7 are shown) and the P cases (middle). (right) Individual moistening tendencies of the P-CTL and P+4K simulations.

cloud-base height remain similar. Some deeper clouds develop that reach depths above 7 km. These deeper clouds increase relative humidity above 3 km and weaken the inversion, but have no strong imprint on the mean profiles of cloud fraction and liquid water.

Even though relative humidity is reduced only little in P+4K, cloud fractions reduce by ∼11.5% relative to P-CTL between about 1 and 3.2 km. This reduction is caused by clouds being more concentrated in the warmer climate, carrying the same amount of liquid over smaller areas, what $q_{l,\,cld}$ is proof of (Figure 6). Between 1.8 and 3.2 km, the reduction is also consistent with a somewhat weaker inversion, which reduces the accumulation of cloud below the inversion. Because the contribution of the deeper clouds to cloud fraction above 3.2 km is small, total cloud cover reduces by ∼1.5% with warming (Table 2). Similar to the non-precipitating case, the albedo decreases from 0.080 to 0.071 in spite of a slight increase in liquid water path. Whereas changes in the vertical distribution of clouds may be more pronounced, the small magnitude of the overall reduction in cloud cover and albedo emphasizes that the real story may more be the robustness of the low clouds with warming, rather than their change.

The small sensitivity of cloud-base cloud fraction to warming is apparent in both the P and noP case (see cfrac_{max} in Table 2). The same was shown in the LES intercomparison of *Blossey et al*. [2013; see their Figure 22], but stands in contrast to the behavior of parameterizations in climate models that mainly reduce cloud fraction close to the base of the shallow clouds [*Brient et al*., 2015]. Moreover, *Brient et al*. [2015] note that models with large cloud fractions near the lifting condensation level reduce cloudiness more effectively in response to warming, and therefore have a higher climate sensitivity. Observations also show that climate models may not capture the right modes of variability in cloudiness in the present-day climate, namely parameterizations tend to vary cloudiness near the base of the cumulus layer more readily with changes in the large-scale state than is observed [*Nuijens et al*., 2015].

The last plot of Figure 7 shows that the enhanced convective moistening, and not an enhanced precipitation tendency, maintains the equilibrium in the P+4K case. Some more precipitation forms in P+4K from the deeper clouds above 3.2 km, which slightly enhances both the moistening in the cloud layer and surface precipitation (Table 2). The large domain simulations presented in the next section will show that precipitation tendencies change with warming in the presence of deeper convection.

5. Impact of Deeper Convection

To address the hypothesis that convective organization may change the response of shallow clouds to warming, we perform simulations on a 16-fold larger (that is, a $51.2 \times 51.2\ \mathrm{km}^2$) domain. In the first subsection, we show how the spatial organization into larger clusters influences the vertical structure of the trade-wind boundary layer using the CTL simulations. Subsection 5.2 then discusses how this modulates the warming response.

5.1. Influence of Deeper Convection on the Trade-Wind Layer Structure

Whilst the boundary layer deepening and surface fluxes of the Plarge-CTL case develop similarly as on the small domain for the first 2 days, they begin to differ when some deeper clouds form that produce substantial precipitation and trigger large cold pools (see Figure 8). Spreading cold pools trigger subsequent, deeper convection at the cold-pool front through a combination of thermodynamic and dynamic perturbations (something commonly referred to as cold-pool dynamics [e.g., *Schlemmer and Hohenegger*, 2014]). This deeper convection reaches the top of the domain at 10 km already after 2.5 days. Figure 9 shows snapshots of the cloud albedo of the different cases to illustrate the different horizontal structures of the cloud fields. The Plarge-CTL case (d) shows a strong separation into clear and cloudy patches. A spreading cold pool triggers uplift at the cold-pool front, where the subsequent clouds form along the arc-like structure of this front. In contrast to the horizontal structures found in Plarge-CTL, both the noP-CTL (a) and P-CTL (b) simulations show little evidence of spatial organization. The larger clouds producing substantial precipitation on the small domain still generate cold pools, but the domain is too small for these cold pools to introduce an organization of the temperature and humidity field.

Because the development of deeper convection in Plarge-CTL may be somewhat artificial, we performed a simulation with a uniform 4 K cooling at constant relative humidity (see Table 1). The surface latent heat flux of this simulation is 190 W m^{-2} and indeed, no clouds deeper than 6.5 km form (not shown).

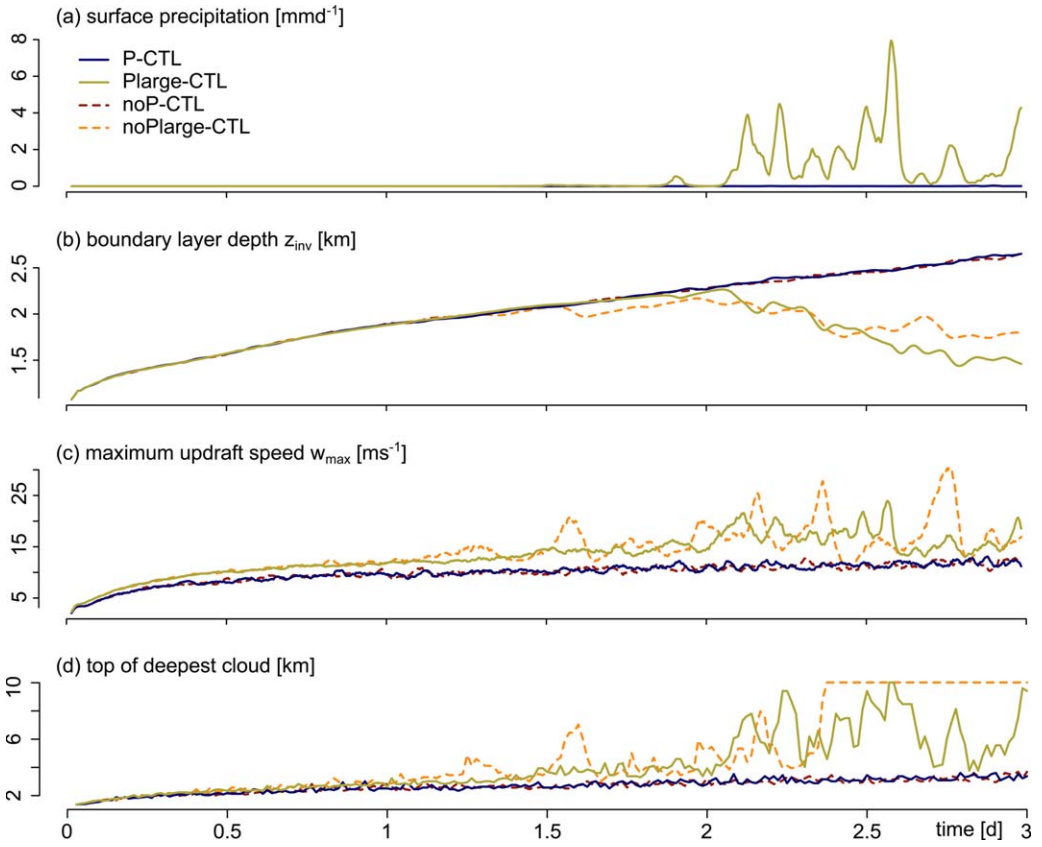

Figure 8. Domain-averaged time series for the precipitating (solid) and nonprecipitating (dashed) CTL cases on the small (12.8 × 12.8 km^2) and large (51.2 × 51.2 km^2) domain.

Nevertheless, the clouds reaching up to about 6 km in the Plarge–4K case represent larger and deeper clusters that influence the trade-wind layer in a similar way as the 10 km deep clouds in Plarge-CTL. The idea that the development of much deeper convection in Plarge-CTL may be artificial is also explored by relaxing some of the assumptions in the simplified setup. Not only the latent heat fluxes, but also the uniform radiative cooling of -2.5 K d^{-1} in the free troposphere represents a strong forcing promoting the development of deeper clouds. In an additional simulation of Plarge-CTL with interactive radiation (IRAD Plarge, see Table 1 for further specifications), radiative cooling in the free troposphere reduces by 1–1.5 K d^{-1}, which stabilizes the free troposphere and suppresses deep convection (see the dotted black line in Figure 10). The transition to deeper convection, and its surprising sensitivity to domain size, clearly merits more study [see e.g., *Kuang and Bretherton*, 2006; *Böing et al*., 2012 for investigations into the transition from shallow to deep cumulus convection]. Here we simply take advantage of the simulations to study the impact of deeper convection on the equilibrium trade-wind layer structure and warming response, the main purpose of this work.

The profiles in Figure 10 show a strong impact of the presence of deeper clouds on the thermodynamic structure of the trade-wind layer. Comparing the two CTL simulations (solid lines), we find that the trade-wind clouds become much shallower in Plarge-CTL. Whereas the deep clouds increase relative humidity beyond 8 km, the shallower trade-wind layer becomes much drier. Both the temperature and humidity lapse rates are larger and the trade-wind layer thus more stable. The drier layer results in less condensate-laden clouds, with lower cloud fraction throughout the shallow cloud layer, albeit least pronounced near cloud base, consistent with the previous results. The liquid water path and total cloud cover decrease to 25 g m^{-2} and 9.1%, respectively, (see Table 3) and the albedo reduces from 8% to 4.9%.

Surface precipitation doubles from P-CTL to Plarge-CTL despite a decrease in domain-average liquid water and similar precipitation rates close to the inversion in the two simulations (see Table 3 and

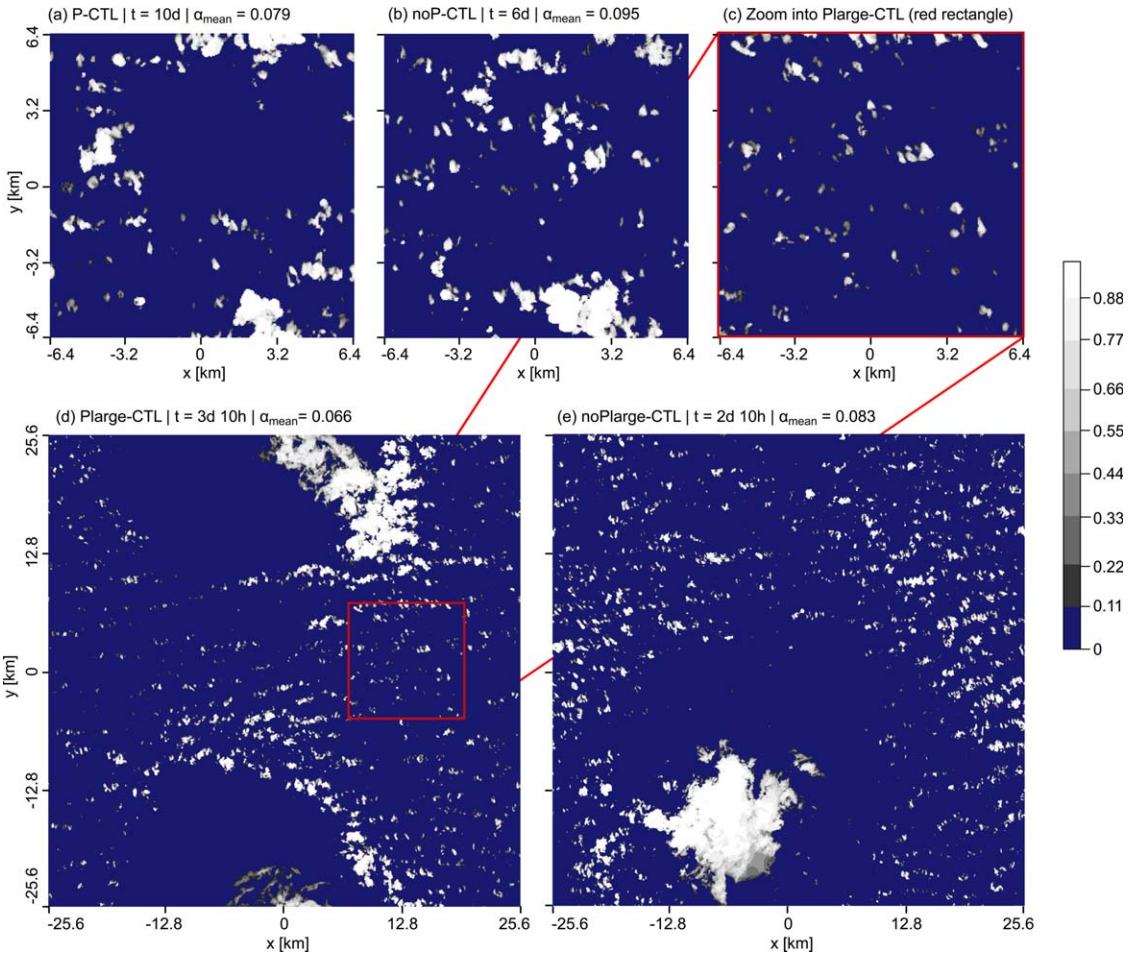

Figure 9. Snapshots of cloud albedo: (a) and (b) show the small domain (12.8 × 12.8 km^2) P-CTL and noP-CTL, (d) and (e) the large (51.2 × 51.2 km^2) domain Plarge-CTL and noPlarge-CTL simulations. (c) Displays a zoom into a 12.8 × 12.8 km^2 region of Plarge-CTL. The recording time and the mean albedo of the respective field are indicated.

Figure 10i). This increase in surface precipitation is associated with a decrease in the number of precipitating columns in the domain. As most of the precipitation comes from the small areas of deep convection, there is a greater distinction between the precipitating and nonprecipitating areas. The larger variance of total water is evidence of a larger contrast in humidity between the clear and cloudy columns. Precipitation from the deeper aggregated clouds tends to fall through moister environments, reducing evaporation in the on-average drier trade-wind layer. By stabilizing the shallow trade-wind layer and enhancing subsidence in the nonprecipitating areas, the deep convection arising from the convective clusters effectively keeps the remainder of the clouds shallow. In energetic terms, the doubling of surface precipitation to 1 mm d^{-1} constitutes about a 15 W m^{-2} reduction of energy compared to P-CTL, which is roughly compensated by the 13 W m^{-2} increase of the latent heat flux. The precipitation characteristics of the Plarge-CTL case are similar to observations during RICO, when average precipitation amounts of 1 mm d^{-1} were observed, with larger rain rates associated with arc-shaped structures forming on what appeared to be cold-pool boundaries [*Rauber et al*., 2007; *Snodgrass et al*., 2009].

The left plot of Figure 11 shows that besides the lowering of the maxima of cooling and moistening in the inversion layer, the moisture source at cloud base is stronger than in the inversion layer for Plarge-CTL. Cloud base moistening is strongly enhanced in the Plarge-CTL case, likely because of the larger stratification across cloud base due to the drier domain-mean cloud layer, which corresponds to larger convective moistening that balances the enhanced subsidence drying. Further, due to the drier subcloud layer, Q_2 is also enhanced below cloud base.

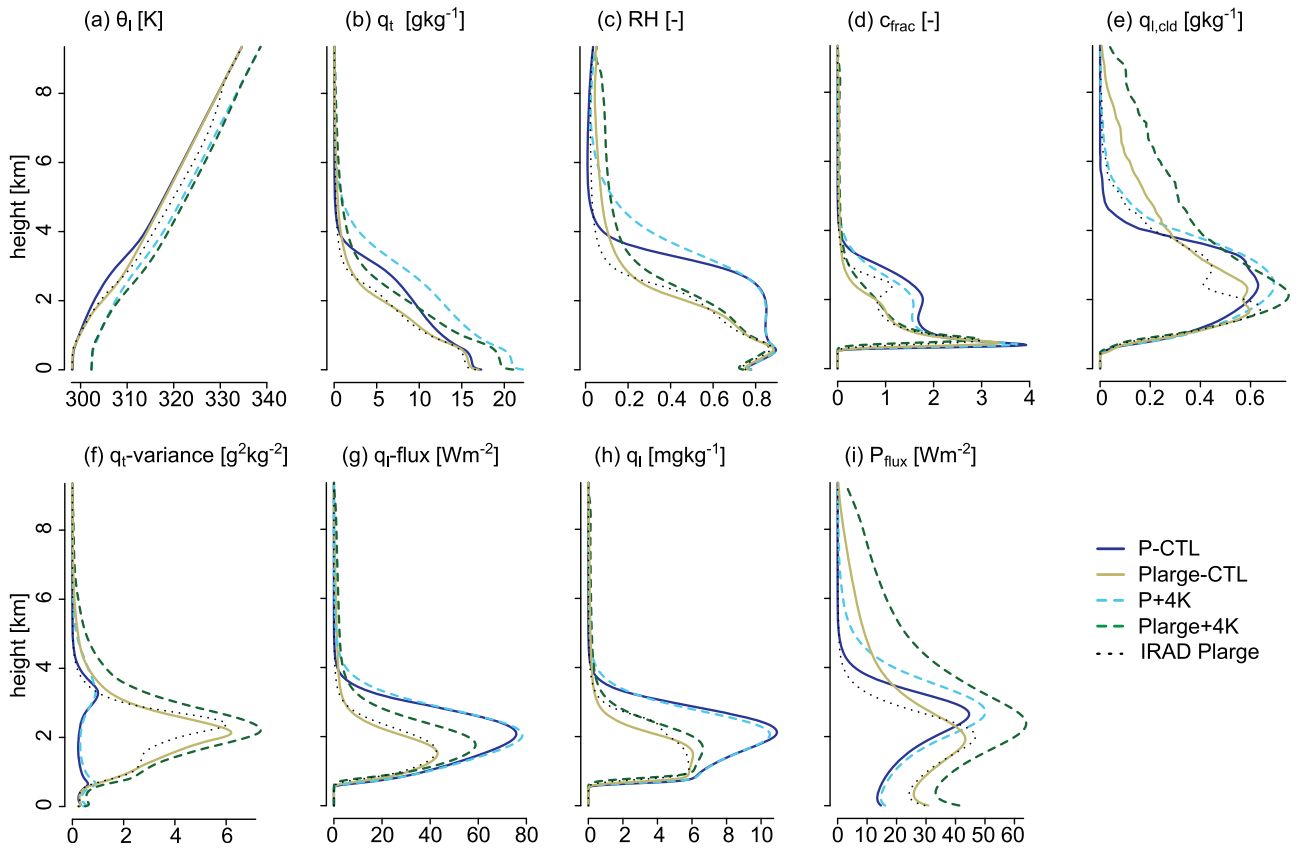

Figure 10. Domain-averaged vertical profiles of the (a) liquid water potential temperature θ_l, (b) total humidity q_t, (c) relative humidity *RH*, (d) cloud fraction c_{frac} (with a zoom into the cloud base region), (e) conditionally averaged cloud water $q_{l,cld}$, (f) variance of total water q_t, (g) liquid water q_l-flux, (h) domain-mean liquid water q_l, and (i) precipitation flux P_{flux}. Shown are again both P and Plarge for the CTL (solid) and the +4K (dashed) climate states, along with the interactive radiation simulation IRAD Plarge (dotted).

Hence, by simulating on a 16-fold larger domain and allowing for mesoscale organization, a very different convection regime emerges, which manifests itself in the thermodynamic structure of the trade-wind layer and in cloudiness and precipitation characteristics.

The warming and drying of the trade-wind layer associated with the emergence of deep convection in the large domain simulation is not exclusive to the precipitating case: also in noPlarge-CTL, deep convection forms, and the trade-wind layer warms and dries (see Figure 8d, and Figure 12e–f in the Appendix). Figure 9e displays a snapshot of noPlarge-CTL, which shows a certain separation of clear and cloudy regions on a scale comparable to the domain size. As the nonprecipitating deep clouds do not generate cold pools, no mesoscale arcs are formed and the effect of deep clouds on their immediate surroundings is less evident than is the case for Plarge-CTL.

The simulations are a reminder that although cold-pool dynamics may often be an important impetus for deep convection, they are not necessary for its development [*Jeevanjee and Romps*, 2013; *Muller and Bony*, 2015], even in situations where we initially did not anticipate the development of deep clouds. There are no cold pools that can trigger deeper convection at colliding cold-pool boundaries, but in the absence of precipitation, more cloud liquid water evaporates and moistens the environment directly surrounding the updraft. Via entrainment, the moister ambient air promotes the deepening of convection through positive moisture-convection feedbacks (see the discussion in Appendix A). Although not directly related to the objectives of this study, one curious aspect of the simulations is why the larger domain allows deeper convection to form, which then completely reorganizes the flow and in particular the thermodynamic structure near the surface. On a larger domain, larger maximum updraft speeds are realized from the beginning of the simulation (see Figure 8c). *Bjerknes* [1938] provides a dynamical argument how stronger and deeper updrafts can be maintained on larger domains, by spreading their compensating subsidence over broader

Table 3. Averages of Surface Latent Heat Flux (LHF), Surface Precipitation Rate (P_{surf}), Integrated Subsidence Drying (D), Integrated Residual Moistening Tendency (DT), Surface Sensible Heat Flux (SHF), Boundary Layer Depth (z_{inv}), Cloud Cover (CC), Liquid Water Path (LWP), Albedo (α), Maximum Cloud Fraction ($cfrac_{max}$), Fraction of Columns With Precipitation (P_{frac}), and Maximum Vertical Velocity (w_{max}); for Small Domain (P) and Large Domain (Plarge) Precipitating Simulations of Both the CTL and +4K Climate States

Case	LHF (Wm^{-2})	P_{surf} ($W\,m^{-2}$)	D ($W\,m^{-2}$)	DT ($W\,m^{-2}$)	SHF (Wm^{-2})	z_{inv} (m)	CC (%)	LWP (gm^{-2})	α (%)	$cfrac_{max}$ (%)	P_{frac} (%)	w_{max} (ms^{-1})
P-CTL	251	15	−236	1	0.7	2633	13.5	36.4	8.0	3.9	1.7	12.2
Plarge-CTL	262	29	−220	12	2.7	1620	9.1	25.0	4.9	3.4	1.0	14.8
P+4K	310	16	−302	−8	−2.3	2056	11.9	40.6	7.1	3.7	1.8	13.0
Plarge+4K	371	42	−281	49	−0.5	1747	7.8	41.1	4.6	3.0	1.3	19.4

areas and therefore reducing the effective stability felt by the updraft. A larger domain may also sample rare events somewhat better, thereby increasing the likelihood of deeper clouds forming somewhere. Both of these mechanisms may play a role and are explored in more detail in Appendix A.

5.2. Warming Response

By permitting the emergence of convective aggregation, the increase of the domain size has a much stronger effect on the trade-wind boundary layer than the 4 K warming itself. Figure 10 shows that the shape of the q_t and θ_l profiles of Plarge-CTL and Plarge+4K are similar, along with more similar relative humidity, liquid water, cloud fraction, q_t–variance, and to some extent also precipitation flux profiles.

With warming, the amount of deep clouds is enhanced on the large domain, as seen from the increased relative humidity beyond 2 km. The deep clouds strongly enhance the precipitation flux and lead to a much stronger increase of surface precipitation with warming on the large domain (see Table 3). From an energetic point of view, this can be understood by noting that the integrated subsidence drying in the dry shallow Plarge+4K trade-wind layer cannot increase enough to balance the strongly enhanced latent heat flux, which implies that larger precipitation drying is needed. Under warming, precipitation therefore has a stronger role in balancing the convective tendencies in the presence of a few deep clouds that effectively shallow and dry the trade-wind layer in regions away from deep convection. One deleterious effect of the deep convection is that longer time and larger spatial scales are introduced, and as a result the simulations are further away from stationarity. The Plarge+4K case has a particularly strong residual moistening tendency of about 49 $W\,m^{-2}$.

Total cloud cover reduces from 9.1% to 7.8% with warming, comparable to the reduction on the small domain (Table 3). Both the weakening of the inversion, reducing the stratiform component near cloud tops (Figure 10d), and the slight reduction of cloud fraction near the cumulus bases contribute to this reduction. Similar to the small-domain precipitating case, the warmer climate state supports larger liquid water contents within clouds (Figure 10e). So although the domain-averaged liquid water increases slightly, the cloud

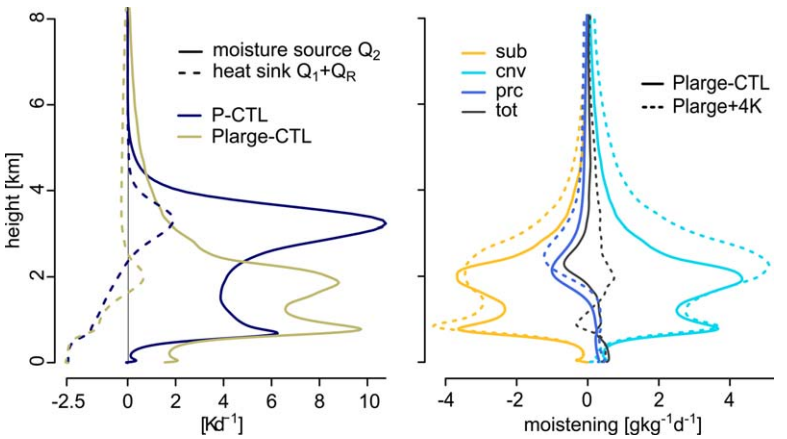

Figure 11. (left) Profiles of the heat sink (Q_1+Q_R, dashed) and moisture source (Q_2, solid) for P-CTL and Plarge-CTL, and (right) the individual moistening tendencies of the Plarge-CTL (solid) and Plarge+4K (dashed).

fraction goes down. Previous LES studies show that entrainment feedbacks can prevent the liquid-water flux from increasing much with a climate perturbation [*Bretherton and Blossey*, 2014]. Namely, the increased buoyancy with larger liquid water content leads to more entrainment across the inversion, and this additional drying and warming can reduce the liquid water content again. This is true for our nonprecipitating simulations (not shown), and also the precipitating small domain simulations show only a small increase in the liquid-water flux with warming (Figure 10g). But on the large domain, an increase in liquid-water flux with warming is much more pronounced, because a few larger and deeper clouds carry most of the liquid across the inversion, making the entrainment feedback far less efficient.

Despite the strong influence of deeper convection on the trade-wind layer structure and dynamics, the overall cloud response to warming, and the processes causing them, remain similar as on the small domain—with the exceptions of the stronger role of precipitation in balancing the enhanced convective moistening and the slight deepening of the trade-wind layer (Table 3). Because the liquid water path increases much more with warming on the large domain (related to the more strongly enhanced latent heat flux), the albedo reduction is smaller. As mentioned in the previous section, we also performed an experiment with a uniform 4 K cooling (at constant relative humidity), which indicates that similar mechanisms act between the CTL and the +4K climate state, and, respectively, the −4K and the CTL climate state (not shown). Moreover, also the mechanisms among the small and large domain simulations are similar, increasing the robustness of the results.

6. Conclusions

The response of shallow trade-wind convection to warming is studied with a special interest in how precipitation and organization of moist convection into deeper clusters modulate this response. Large-eddy simulations representative of present-day trade-wind conditions are compared to runs with a 4 K uniform warming at constant relative humidity. The effect of precipitation is assessed by either allowing or inhibiting the formation of precipitation, and by allowing mesoscale structures associated with precipitation to form through simulations on much larger domains.

As cloud fraction has its maximum near the cumulus bases, the near-base insensitivity to warming present in all cases considered partly masks the more pronounced changes that occur in the vertical distribution of cloud fraction. Different, albeit related mechanisms control the vertical distribution of cloudiness in the presence or absence of precipitation. In the nonprecipitating case, the slight relative drying of the deeper boundary layer in the +4K climate state causes both a reduced cloud fraction between 1.5 and 4 km and a weaker stratiform component at cloud tops. Because of an opposing tendency to convection in the inversion layer and the evaporation of precipitation in the lower cloud layer, precipitation efficiently buffers the warmer cloud layer against deepening and relative drying. Cloud fractions between 1 and 3.2 km still decrease, owing to two mechanisms: (a) the clouds become more concentrated, that is they carry the same amount of liquid over a smaller area, and (b) the inversion weakens, reducing the stratiform cloud component in the inversion layer. Previous studies pointed out the importance of precipitation in limiting the boundary layer deepening with warming and thereby affecting the sensitivity of shallow cumulus clouds to climate perturbations [*Bretherton et al*., 2013; *Blossey et al*., 2013]. Here, we link these ideas to processes that maintain the budgets of heat and moisture. We find that convective moistening in the warmer climate state, fueled by the larger latent heat flux, increases strongly to balance the enhanced subsidence drying caused by the increased humidity gradient between the surface and the free troposphere. The precipitation drying only replaces subsidence drying as the latter becomes less effective in the presence of a few deeper cloud clusters and an overall shallower and drier trade-wind layer on the large domain.

Overall, the increase of domain size—and thus the spatial organization of shallow convection into larger and deeper clusters—has a much stronger effect on the trade-wind layer than the 4 K warming. Simulations with the same setup on a 16-fold larger domain (51.2×51.2 km^2) support the spatial organization of clouds into clusters that get as deep as the domain top at 10 km. By stabilizing the boundary layer and enhancing subsidence in the nonprecipitating areas, the presence of the deeper clouds results in a shallower, drier, and warmer equilibrium trade-wind layer. Also the moisture source (Q_2) and heat sink ($Q_1 + Q_R$) are altered, with a strongly enhanced moisture source in the subcloud layer, at cloud base and above the trade-wind layer inversion. The emergence of deep convection on larger domains, although unintended and perhaps somewhat

sensitive to the case setup, renders closer to observations the thermodynamic structure of the large domain precipitating control simulation, its precipitation characteristics, and horizontal structure [e.g., *Rauber et al.*, 2007; *Zuidema et al.*, 2012; *Stevens et al.*, 2016]. The development of larger and deeper clouds in larger domain simulations is not exclusive to precipitating simulations, but also occurs in the nonprecipitating large domain case, with a similar influence on the thermodynamic structure of the trade-wind layer. In the absence of cold pools, moisture-convection feedbacks strengthen and the updrafts developing in moister regions preconditioned by previous convection continue to be strong, by entraining moister ambient air.

With warming, cloud cover and albedo decrease in all cases considered. This would, all else being equal, constitute a positive cloud feedback in the shallow cumulus regime. The albedo thereby decreases in spite of increasing liquid water paths, because reductions in total cloud cover tend to more than offset increases in liquid water. Nevertheless, the albedo reductions are small. If we take the global average cloud radiative effects of about -20 W m^{-2} [*Boucher et al.*, 2013] as representative of trade-wind regimes (assumed to cover a third of the oceans), and suppose changes in cloud radiative effects scale with changes in albedo, then we see a 6–11% reduction in cloud radiative effects in our precipitating simulations for a 4 K warming. The lower and upper bound of this reduction stem from the different albedo reductions in the large and small domain simulations, respectively. The simple calculation thus gives us a change in cloud radiative effects of about 0.1–0.18 W m^{-2} K^{-1}, that is, a robustly positive but likely much smaller change than one finds in global models [*Boucher et al.*, 2013]. A particular insensitivity to warming is found for cloudiness near the base of the cumulus layer. This is in line with recent observations [*Nuijens et al.*, 2015], but in contrast to some global models which reduce cloudiness near cumulus bases more readily with warming and therefore suggest a high climate sensitivity [*Brient et al.*, 2015]. Our simplified setup exposes important mechanisms shaping the warming response of precipitating shallow convection, and confirms previous studies suggesting a positive radiative feedback in the shallow cumulus regime. But our results indicate that the positive feedback is likely to be small, which is a demonstration of the insensitivity of precipitating shallow convection to changes in the environment. This insensitivity is shown to persist even in the presence of deep convection that substantially changes the structure of the trade-wind layer in larger domain simulations.

Appendix A: Development of Deep Convection in the Absence of Cold Pools

We mentioned in section 5.1 that cold-pool dynamics and moisture-convection feedbacks lead to the organization and deepening of precipitating and nonprecipitating shallow convection, respectively. Here we explore some factors that might explain why the development of deep convection appears to be so sensitive to domain size. But before doing so, it is worth pointing out that the basic sensitivity to domain size likely reflects the marginal sensitivity of the basic setup. Simulations with interactive radiation, or perhaps with a more realistic profile of imposed warming, may not show similar sensitivities.

Whereas the mean cloud core velocity and mass-flux are initially the same across the simulations on the different domains (not shown), the maximum updraft speed w_{max} is systematically larger in the large domain simulations from its start, independent of precipitation (Figure 8c). There are two possible explanations for this, (a) updrafts interact differently on the large domain (dynamical argument), or (b) the presence of 16$\times$ more updrafts on a 16-fold larger domain may allow for a better sampling of the vertical velocity probability density function (pdf), the tail of which is represented by w_{max} (sampling argument). To test explanation (b), we perform three additional precipitating simulations on the small domain with different random seeds (see Table 1 for details). By always picking the maximum w_{max} out of the four realizations, we construct a w_{max} time series of a composite 25.6 $\times$ 25.6 km^2 domain simulation which neglects the interaction of updrafts on the four times larger length scale, but better samples the pdf. The time series in Figure 12a show w_{max} time series of the precipitating simulations on the first half day. A gradual increase of the mean w_{max} from the small domain cases to the composite 25.6 $\times$ 25.6 km^2 case, the large domain 51.2 $\times$ 51.2 km^2 and an even larger 102.4 $\times$ 102.4 km^2 domain case (Table 1) is evident. Note that a running average is applied to smooth the time series, such that the strong temporal variability of w_{max} is only evident from the zoom in, showing how the 25.6 $\times$ 25.6 km^2 case is indeed a composite of the small domain cases. We conclude from this compositing test that it is the better sampling of the vertical velocity pdf which initially leads to larger w_{max} on a larger domain.

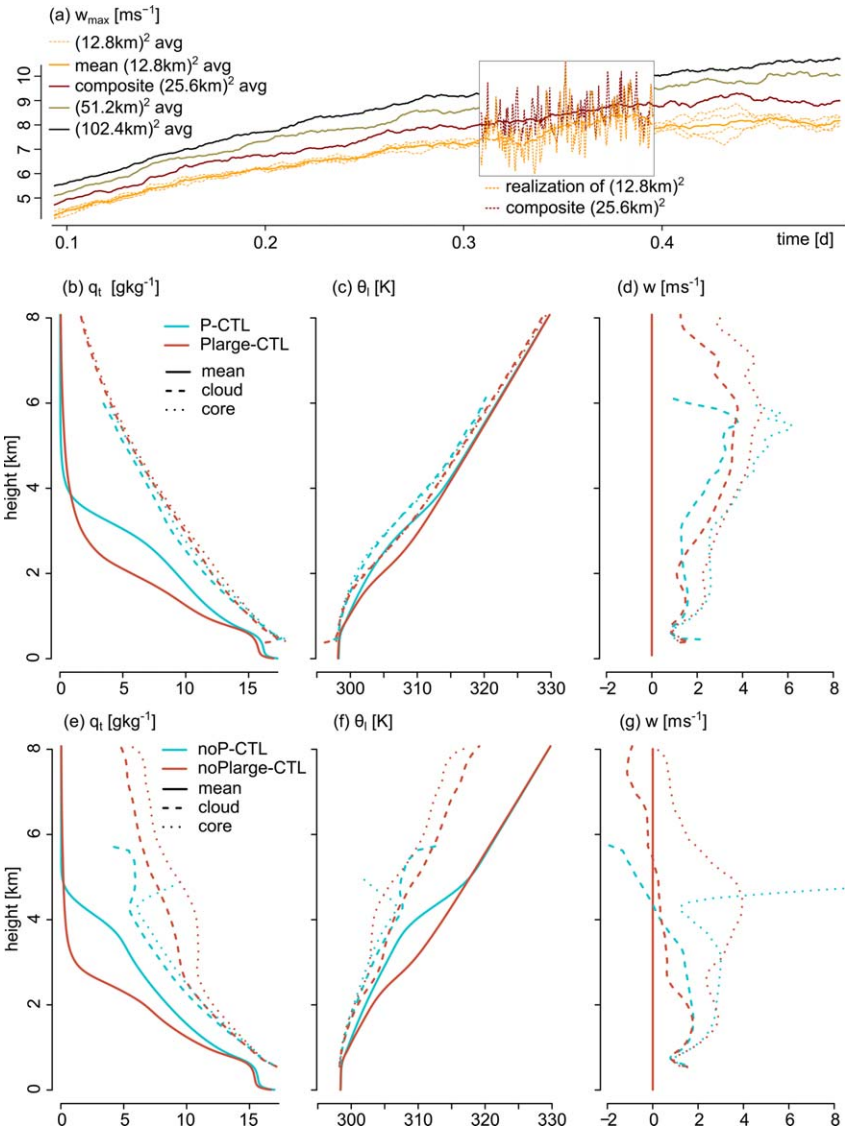

Figure 12. (a) Zoom into the maximum updraft speed w_{max} time series of the first half day. Shown are four realizations of the small (12.8 km)^2 domain P-CTL case with different random seeds, their mean, the composite (25.6 km)^2 case representing the maxima of the four small domain realizations, the Plarge-CTL case on the (51.2 km)^2 domain, and a 4× larger (102.4 km)^2 precipitating CTL case. "avg" stands for time series smoothed with a 30 min running average, the time series highlighted in the zoom in contain the full temporal variability. (b-g) Domain (solid), cloud (dashed), and core (dotted)-averaged profiles of total humidity q_t (b,e), liquid water potential temperature θ_l (c,f), and vertical velocity w (d,g) for the P-CTL and Plarge-CTL (b-d), and the noP-CTL and noPlarge-CTL simulations (e-g).

Bjerknes [1938] presented a simple theoretical framework for explaining the narrowness of saturated cumulus updrafts ascending through a dry-adiabatically subsiding environment (see also *Randall* [2012] for a similar derivation as follows). It may help understand why on larger domains an individual updraft can increase its buoyancy more effectively than on a small domain, where updrafts experience more competition.

Assuming that the updraft speed w_c scales with buoyancy as follows:

$$w_c \sim B \sim \frac{\partial}{\partial t}\left(T_c - \tilde{T}\right), \tag{A1}$$

where B is the buoyancy, the subscript $(\,)_c$ represents cloudy and $\tilde{(\,)}$ represents clear ambient conditions (Figure 8 shows how closely the w_{max} and the maximum cloud top time series are related, especially from about 1.2 days on). The rate of change of cloud temperature depends on the cooling experienced by the vertical ascent and the heating through condensation

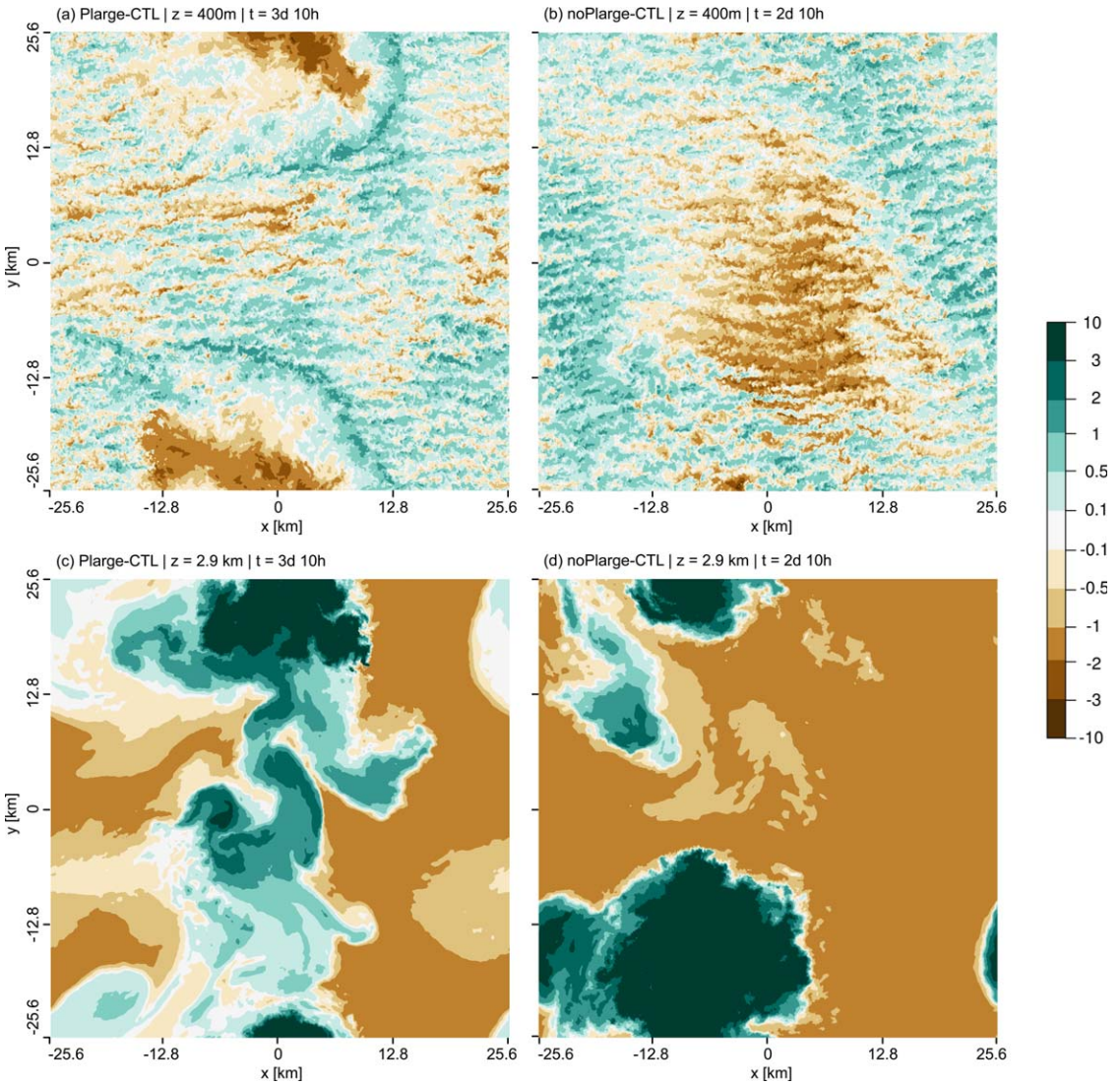

Figure 13. Snapshots of anomalies of total humidity q_t (in g kg^{-1}) at 400 m (a and b) and 2.9 km (c and d) for Plarge-CTL (left) and noPlarge-CTL (right). The snapshots correspond to the cloud fields in Figures 9d and 12e, respectively.

$$\frac{\partial}{\partial t}T_c = w_c(\Gamma - \Gamma_m), \tag{A2}$$

with $\Gamma = -\frac{\partial T}{\partial z}$ being the background lapse rate and Γ_m the moist adiabatic lapse rate. In a clear region, the induced subsiding motion increases the temperature by working against the background stratification by

$$\frac{\partial}{\partial t}\tilde{T} = \tilde{w}(\Gamma - \Gamma_d), \tag{A3}$$

where Γ_d is the dry adiabatic lapse rate and $\tilde{w} < 0$. Satisfying the constraint in LES that

$$\sigma_c w_c + (1-\sigma_c)\tilde{w} = 0 \tag{A4}$$

(σ_c is the fractional area covered by updrafts), the rate at which updrafts gain buoyancy can be written as

$$\frac{\partial}{\partial t}\left(T_c - \tilde{T}\right) = w_c(\Gamma - \Gamma_m) - \tilde{w}(\Gamma - \Gamma_d) = \frac{w_c}{1-\sigma_c}[\Gamma - \Gamma_m - \sigma_c(\Gamma_d - \Gamma_m)]. \tag{A5}$$

In case of conditional instability ($\Gamma - \Gamma_m > 0$ and $\Gamma - \Gamma_d < 0$), updrafts can gain more buoyancy with larger w_c or weaker $\tilde{w}$, both of which can be achieved for $\sigma_c \to 0$, that is, by making the updraft narrow and the

clear neighboring subsiding regions broad. Through this mechanism, updrafts of a given area may develop greater buoyancy on a larger domain, as their compensating subsidence will be spread over a larger area.

Concerning the deepening of convection in the absence of precipitation and cold-pool dynamics, moisture-convection feedbacks [*Bretherton et al*., 2005] appear to play a role. Figures 12b–12g show profiles of cloud-averaged (nonzero liquid water) and cloud core-averaged (nonzero liquid water and positively buoyant compared to slab-average) fields. Although the mean trade-wind layers are drier, the cloud and core-averaged profiles in the large-domain cases are moister than in the respective small domain cases. The differences are particularly strong in noPlarge-CTL, which shows very moist cloud and core-averaged profiles above 2.5 km. Snapshots of the humidity fields in the subcloud and cloud layer (Figure 13) show that moist cloud layers are collocated with moist subcloud layers in noPlarge-CTL. Contrastingly, in Plarge-CTL, cold pools are dry pools located below an anomalously moist cloud layer where convection occurred earlier. Note that while moisture-convection feedbacks strengthen, the strong liquid water loading in noPlarge-CTL likely puts an upper limit to the deepening of convection. The strong liquid water loading manifests itself both in the reduced θ_l compared to the mean (Figure 12f) and in the reduced core-averaged vertical velocity above about 4.5 km (Figures 12d and 12g).

In summary, in the absence of cold pools (and wind shear), moist regions overlap more favorably and, via entrainment, promote the deepening of convection through positive moisture-convection feedbacks.

Acknowledgments

The technical help of Linda Schlemmer with the UCLA LES was greatly appreciated. We acknowledge helpful discussions with Axel Seifert and Sandrine Bony. Constructive comments from Ann Kristin Naumann, Paquita Zuidema, and two anonymous reviewers greatly improved the presentation of the main ideas. The UCLA LES model is distributed under the GNU General Public License and can be downloaded from https://github.com/uclales/uclales. The specific model code, input files and analysis scripts are available on request from publications@mpimet.mpg.de.

References

Albrecht, B. A. (1993), Effects of precipitation on the thermodynamic structure of the trade-wind boundary layer, *J. Geophys. Res.*, *98*(D4), 7327–7337, doi:10.1029/93JD00027.

Bellon, G., and O. Geoffroy (2016), Stratocumulus radiative effect, multiple equilibria of the well-mixed boundary layer and transition to shallow convection, *Q. J. R. Meteorol. Soc.*, doi:10.1002/qj.2762, in press.

Bellon, G., and B. Stevens (2012), Using the sensitivity of large-eddy simulations to evaluate atmospheric boundary layer models, *J. Atmos. Sci.*, *69*(5), 1582–1601, doi:10.1175/JAS-D-11-0160.1.

Betts, A. K. (1973), Non-precipitating cumulus convection and its parameterization, *Q. J. R. Meteorol. Soc.*, *99*(419), 178–196, doi:10.1002/qj.49709941915.

Bjerknes, J. (1938), Saturated-adiabatic ascent of air through dry-adiabatically descending environment, *Q. J. R. Meteorol. Soc.*, *64*, 325–330.

Blossey, P. N., C. S. Bretherton, M. Zhang, A. Cheng, S. Endo, T. Heus, Y. Liu, A. P. Lock, S. R. de Roode, and K.-M. Xu (2013), Marine low cloud sensitivity to an idealized climate change: The CGILS LES intercomparison, *J. Adv. Model. Earth Syst.*, *5*, 234–258, doi:10.1002/jame.20025.

Böing, S. J., H. J. J. Jonker, A. P. Siebesma, and W. W. Grabowski (2012), Influence of the subcloud layer on the development of a deep convective ensemble, *J. Atmos. Sci.*, *69*(9), 2682–2698, doi:10.1175/JAS-D-11-0317.1.

Bony, S., and J.-L. Dufresne (2005), Marine boundary layer clouds at the heart of tropical cloud feedback uncertainties in climate models, *Geophys. Res. Lett.*, *32*, L20806, doi:10.1029/2005GL023851.

Boucher, O., et al. (2013), *Clouds and Aerosols*, section 7, pp. 571–658, Cambridge Univ. Press, Cambridge, U. K., doi:10.1017/CBO9781107415324.016.

Bretherton, C. S., and P. N. Blossey (2014), Low cloud reduction in a greenhouse-warmed climate: Results from Lagrangian les of a subtropical marine cloudiness transition, *J. Adv. Model. Earth Syst.*, *6*, 91–114, doi:10.1002/2013MS000250.

Bretherton, C. S., P. N. Blossey, and M. Khairoutdinov (2005), An energy-balance analysis of deep convective self-aggregation above uniform sst, *J. Atmos. Sci.*, *62*(12), 4273–4292, doi:10.1175/JAS3614.1.

Bretherton, C. S., P. N. Blossey, and C. R. Jones (2013), Mechanisms of marine low cloud sensitivity to idealized climate perturbations: A single-LES exploration extending the CGILS cases, *J. Adv. Model. Earth Syst.*, *5*, 316–337, doi:10.1002/jame.20019.

Brient, F., T. Schneider, Z. Tan, S. Bony, X. Qu, and A. Hall (2015), Shallowness of tropical low clouds as a predictor of climate models response to warming, *Clim. Dyn.*, 1–17, doi:10.1007/s00382-015-2846-0.

Burdanowitz, J., L. Nuijens, B. Stevens, and C. Klepp (2015), Evaluating light rain from satellite- and ground-based remote sensing data over the subtropical North Atlantic, *J. Appl. Meteorol. Climatol.*, *54*(3), 556–572, doi:10.1175/JAMC-D-14-0146.1.

Emanuel, K., A. A. Wing, and E. M. Vincent (2014), Radiative-convective instability, *J. Adv. Model. Earth Syst.*, *6*, 75–90, doi:10.1002/2013MS000270.

Fermepin, S., and S. Bony (2014), Influence of low-cloud radiative effects on tropical circulation and precipitation, *J. Adv. Model. Earth Syst.*, *6*, 513–526, doi:10.1002/2013MS000288.

Fu, Q., and K. N. Liou (1992), On the correlated k-distribution method for radiative transfer in nonhomogeneous atmospheres, *J. Atmos. Sci.*, *49*, 2139–2156.

Holland, J. Z., and E. M. Rasmusson (1973), Measurements of the atmospheric mass, energy, and momentum budgets over a 500-kilometer square of tropical ocean, *Mon. Weather Rev.*, *101*(1), 44–57.

Jeevanjee, N., and D. M. Romps (2013), Convective self-aggregation, cold pools, and domain size, *Geophys. Res. Lett.*, *40*, 994–998, doi:10.1002/grl.50204.

Kuang, Z., and C. S. Bretherton (2006), A mass flux scheme view of a high-resolution simulation of transition from shallow to deep cumulus convection, *J. Atmos. Sci.*, *63*, 1895–1909.

Li, Z., P. Zuidema, P. Zhu, and H. Morrison (2015), The sensitivity of simulated shallow cumulus convection and cold pools to microphysics, *J. Atmos. Sci.*, *72*(9), 3340–3355, doi:10.1175/JAS-D-14-0099.1.

Muller, C., and S. Bony (2015), What favors convective aggregation and why?, *Geophys. Res. Lett.*, *42*, 5626–5634, doi:10.1002/2015GL064260.

Muller, C. J., and I. M. Held (2012), Detailed investigation of the self-aggregation of convection in cloud-resolving simulations, *J. Atmos. Sci.*, *69*(8), 2551–2565, doi:10.1175/JAS-D-11-0257.1.

Nuijens, L., and B. Stevens (2012), The influence of wind speed on shallow marine cumulus convection, *J. Atmos. Sci.*, *69*(1), 168–184, doi: 10.1175/JAS-D-11-02.1.
Nuijens, L., B. Stevens, and A. P. Siebesma (2009), The environment of precipitating shallow cumulus convection, *J. Atmos. Sci.*, *66*, 1962–1979.
Nuijens, L., B. Medeiros, I. Sandu, and M. Ahlgrimm (2015), The behavior of trade-wind cloudiness in observations and models: The major cloud components and their variability, *J. Adv. Model. Earth Syst.*, *7*, 600–616, doi:10.1002/2014MS000390.
Pincus, R., and B. Stevens (2009), Monte Carlo spectral integration: A consistent approximation for radiative transfer in large eddy simulations, *J. Adv. Model. Earth Syst.*, *1,1*, doi:10.3894/JAMES.2009.1.1.
Randall, D. A. (2012), Why are cumulus updrafts narrow?. [Available at http://kiwi.atmos.colostate.edu/group/dave/at745/Cumulus_Updrafts_Narrow.pdf, accessed on 21 Sep.2015]
Rauber, R. M., et al. (2007), Rain in shallow cumulus over the ocean: The RICO campaign, *Bull. Am. Meteorol. Soc.*, *88*(12), 1912–1928, doi: 10.1175/BAMS-88-12-1912.
Rieck, M., L. Nuijens, and B. Stevens (2012), Marine boundary layer cloud feedbacks in a constant relative humidity atmosphere, *J. Atmos. Sci.*, *69*(8), 2538–2550, doi:10.1175/JAS-D-11-0203.1.
Savic-Jovcic, V., and B. Stevens (2008), The structure and mesoscale organization of precipitating stratocumulus, *J. Atmos. Sci.*, *65*(5), 1587–1605, doi:10.1175/2007JAS2456.1.
Schlemmer, L., and C. Hohenegger (2014), The Formation of Wider and Deeper Clouds as a Result of Cold-Pool Dynamics, *J. Atmos. Sci.*, *71*(8), 2842–2858, doi:10.1175/JAS-D-13-0170.1.
Seifert, A., and K. D. Beheng (2001), A double-moment parameterization for simulating autoconversion, accretion and self-collection, *Atmos. Res.*, *59–60*, 265–281.
Seifert, A., and T. Heus (2013), Large-eddy simulation of organized precipitating trade-wind cumulus clouds, *Atmos. Chem. Phys.*, *13*(11), 5631–5645, doi:10.5194/acp-13-5631-2013.
Seifert, A., T. Heus, R. Pincus, and B. Stevens (2015), Large-eddy simulation of the transient and near-equilibrium behavior of precipitating shallow convection, *J. Adv. Model. Earth Syst.*, *7*, 1918–1937, doi:10.1002/2015MS000489.
Sherwood, S. C., S. Bony, and J.-L. Dufresne (2014), Spread in model climate sensitivity traced to atmospheric convective mixing, *Nature*, *505*(7481), 37–42, doi:10.1038/nature12829.
Short, D. A., and K. Nakamura (2000), TRMM radar observations of shallow precipitation over the tropical oceans, *J. Clim.*, *13*(23), 4107–4124, doi:10.1175/1520-0442(2000)013 < 4107:TROOSP > 2.0.CO;2.
Siebert, H., et al. (2013), The fine-scale structure of the trade-wind cumuli over Barbados—an introduction to the CARRIBA project, *Atmos. Chem. Phys.*, *13*(19), 10,061–10,077, doi:10.5194/acp-13-10061-2013.
Snodgrass, E. R., L. Di Girolamo, and R. M. Rauber (2009), Precipitation characteristics of trade-wind clouds during RICO derived from radar, satellite, and aircraft measurements, *J. Appl. Meteorol. Climatol.*, *48*, 464–483.
Stevens, B. (2007), On the growth of layers of nonprecipitating cumulus convection, *J. Atmos. Sci.*, *64*(8), 2916–2931, doi:10.1175/JAS3983.1.
Stevens, B., and A. Seifert (2008), Understanding macrophysical outcomes of microphysical choices in simulations of shallow cumulus convection, *J. Meteorol. Soc. Jpn*, *86A*, 143–162, doi:10.2151/jmsj.86A.143.
Stevens, B., et al. (2005), Evaluation of large-eddy simulations via observations of nocturnal marine stratocumulus, *Mon. Weather Rev.*, *133*(6), 1443–1462, doi:10.1175/MWR2930.1.
Stevens, B., et al. (2016), The Barbados cloud observatory: Anchoring investigations of clouds and circulation on the edge of the ITCZ, *Bull. Am. Meteorol. Soc.*, doi:10.1175/BAMS-D-14-00247.1, in press.
Tiedtke, M. (1989), A comprehensive mass flux scheme for cumulus parameterization in large-scale models, *Mon. Weather Rev.*, *117*, 1779–1800.
VanZanten, M. C., et al. (2011), Controls on precipitation and cloudiness in simulations of trade-wind cumulus as observed during RICO, *J. Adv. Model. Earth Syst.*, *3*, M06001, doi:10.1029/2011MS000056.
Vial, J., J. L. Dufresne, and S. Bony (2013), On the interpretation of inter-model spread in CMIP5 climate sensitivity estimates, *Clim. Dyn.*, 3339–3362, doi:10.1007/s00382-013-1725-9.
Yanai, M., S. Esbensen, and J.-H. Chu (1973), Determination of bulk properties of tropical cloud clusters from large-scale heat and moisture budgets, *J. Atmos. Sci.*, *30*, 611–627.
Zhang, Y., B. Stevens, and M. Ghil (2005), On the diurnal cycle and susceptibility to aerosol concentration in a stratocumulus-topped mixed layer, *Q. J. R. Meteorol. Soc.*, *131*(608), 1567–1583, doi:10.1256/qj.04.103.
Zhao, M. (2014), An investigation of the connections among convection, clouds, and climate sensitivity in a global climate model, *J. Clim.*, *27*(5), 1845–1862, doi:10.1175/JCLI-D-13-00145.1.
Zuidema, P., Z. Li, R. J. Hill, L. Bariteau, B. Rilling, C. Fairall, W. A. Brewer, B. Albrecht, and J. Hare (2012), On trade-wind cumulus cold pools, *J. Atmos. Sci.*, *69*(1), 258–280, doi:10.1175/JAS-D-11-0143.1.